
(This is a sample cover image for this issue. The actual cover is not yet available at this time.)

Earth and Planetary Science Letters 364 (2013) 59–67

Contents lists available at SciVerse ScienceDirect

Earth and Planetary Science Letters

journal homepage: www.elsevier.com/locate/epsl

# Mega ultra low velocity zone and mantle flow

Michael S. Thorne [a,*], Edward J. Garnero [b], Gunnar Jahnke [c], Heiner Igel [c], Allen K. McNamara [b]

[a] Department of Geology and Geophysics, University of Utah, Salt Lake City, UT 84112, USA
[b] School of Earth and Space Exploration, Arizona State University, Tempe, AZ 85287, USA
[c] Department of Earth and Environmental Sciences, Ludwig-Maximilians Universität, Theresienstrasse 41, 80333 Munich, Germany

ARTICLE INFO

*Article history:*
Received 13 May 2011
Received in revised form
26 December 2012
Accepted 27 December 2012
Editor: Y. Ricard

*Keywords:*
ULVZ
LLSVPS
core-mantle boundary
seismic wave propagation
mantle convection

ABSTRACT

Mantle flow in Earth's interior has been inferred from a variety of geo-disciplines. Two continental-scale, nearly antipodal, large low shear velocity provinces (LLSVPs) at the base of the mantle, thought to be dense and chemically distinct likely play a significant role in mantle dynamics and plume generation, and hence are targeted in a high-resolution seismic study. We analyze broadband SPdKS waveforms using a 2.5D axi-symmetric finite difference wave propagation algorithm PSVaxi. Here we find patches of greatly reduced seismic wave speeds at the core–mantle boundary, i.e., ultra-low velocity zones (ULVZs), within the Pacific LLSVP, including the largest ULVZ detected to date, roughly $250 \times 800$ km in lateral dimension and 10–15 km thick, in an apparent hole in the LLSVP. The presence of this ULVZ in the LLSVP hole is well explained by dynamically merging, chemically-distinct piles containing ULVZs at their margins. The consequence of these merging piles may be to initiate anomalously large, infrequent plumes, as well as to provide a means to transfer isotopes to the surface.


## 1. Introduction

Complex structures at Earth's core–mantle boundary (CMB) relate to and govern important phenomena at mantle-wide scales, such as heat flow from the core and the related cooling of Earth, patterns and vigor of plume upwelling, and long-lived presumed primitive deep mantle reservoirs (Hofmann, 1997; Jellinek and Manga, 2004; McNamara and Zhong, 2005; Thompson and Tackley, 1998). Lowermost mantle heterogeneity at long wavelengths ($>1000$ km) is dominated by two large low shear velocity provinces (LLSVPs), one beneath the Pacific Ocean and one beneath Africa and the Atlantic Ocean (Becker and Boschi, 2002; Grand, 2002; Gu et al., 2001; Mégnin and Romanowicz, 2000; Ritsema and van Heijst, 2000). LLSVPs possess lower-than-average shear wave velocities compared to the surrounding mantle, with suggestions of elevated density (Ishii and Tromp, 2004; Trampert et al., 2004). The margins between LLSVPs and the surrounding mantle appear seismically sharp (Bréger and Romanowicz, 1998; Ford et al., 2006; He and Wen, 2009; He et al., 2006; Luo et al., 2001; Sun et al., 2009; To et al., 2005). These observations support the proposition that LLSVPs are chemically distinct and slightly negatively or neutrally buoyant thermochemical piles (Deschamps and Tackley, 2009; McNamara and Zhong, 2004, 2005; Nakagawa et al., 2010; Tackley, 2002).

Directly above the CMB in LLSVP regions, thin (5–40 km) and laterally isolated ($<100$ km) patches of mantle rock exhibit P- and S-wave velocity reductions of 10% and greater (Idehara, 2011; Idehara et al., 2007; Rost et al., 2005; Thorne and Garnero, 2004). S-wave reductions are often reported as approximately 3 times stronger than that of P-wave reductions (e.g., up to 30%), which is well explained by the presence of partial melt (Berryman, 2000; Williams and Garnero, 1996). Called ultra-low velocity zones (ULVZs), this material remains stable at the CMB if it possesses increased density, either from a chemically distinct source (McNamara et al., 2010) and/or the melt phase being denser than the solid (Hernlund and Jellinek, 2010; Nomura et al., 2011).

The surface locations of hot spot volcanism preferentially overlie LLSVP edges (Burke, 2011; Thorne et al., 2004; Torsvik et al., 2006). ULVZs have also been found in the vicinity of LLSVP boundaries (He et al., 2006; Rost et al., 2005), and have thus been suggested to play an important role in plume genesis, hotspot volcanism, and perhaps the formation of large igneous provinces (Garnero and McNamara, 2008; Rost et al., 2005; Torsvik et al., 2006). Geodynamic simulations have demonstrated the dynamic feasibility of ULVZ accumulation at the margins of thermochemical piles (McNamara et al., 2010), with plume initiation preferentially at the peaks of piles. If the sides of chemically distinct piles are relatively steep, a factor that depends on rheology, chemistry, and convective strength, then plumes tend to be in close proximity to pile margins. The present-day structure, geometry, and geographical relationship between seismically imaged ULVZs and LLSVPs, therefore, contain key information

* Corresponding author. Tel.: +1 801 585 9792.
*E-mail address:* michael.thorne@utah.edu (M.S. Thorne).

0012-821X/$ - see front matter © 2013 Elsevier B.V. All rights reserved.
http://dx.doi.org/10.1016/j.epsl.2012.12.034

on deep mantle convective forces that shape them, and hence, past subduction in the circum-Pacific.

The Pacific is an ideal region for studying both LLSVP and ULVZ structure, due to the relative abundance of circum-Pacific recording stations and deep focus earthquakes. In fact, this region has been more extensively investigated for ULVZs than anywhere on Earth using a variety of seismic probes (McNamara et al., 2010; Thorne and Garnero, 2004). However, precise ULVZ physical dimensions and elastic properties are not well constrained in many studies due to inadequate or smeared ray path coverage and/or modeling tradeoffs from use of 1-D waveform modeling tools to resolve 3-D structure (Garnero and Helmberger, 1998).

The confluence of two fundamental advances in seismology makes high resolution ULVZ modeling for this region possible: (1) a wealth of new data has become available as seismic networks expand, such as in N. America over the past 8 years through the addition of the Transportable Array component of EarthScope's USArray (USArray) and additions to the Advanced National Seismic System backbone of seismometers; and (2) increased availability of distributed computing resources enabling the simulation of global seismograms in 2+ dimensions. Here we investigate ULVZ structure beneath the southwest Pacific Ocean using the seismic phase SPdKS and high resolution synthetic seismogram modeling in 2.5D dimensions.

## 2. Data

We utilize SPdKS, an SKS wave that intersects the CMB at the critical angle for SV-to-P energy conversion, yielding horizontally propagating mantle-side P-diffraction (Pd). Thus SPdKS has short segments of Pd energy that travel on the mantle side of the CMB at the SKS core-entry and exit locations (Fig. 1a). Since the mantle

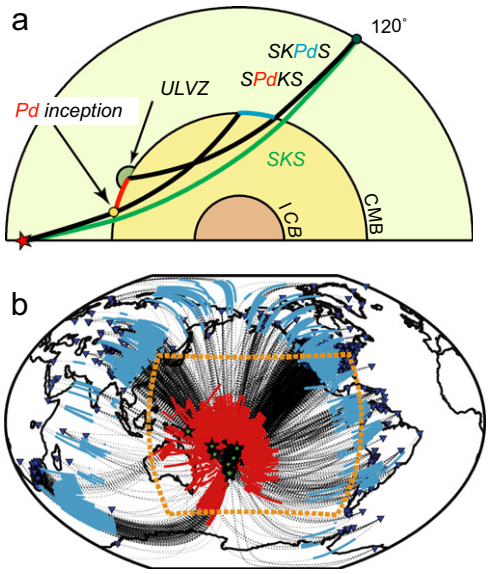


**Fig. 1.** SPdKS ray path geometry and data collected. (a) Ray path geometry of seismic phases SKS (green), SPdKS (black with Pd section red), and SKPdS (black with Pd section blue). The point where the SKS ray intersects the CMB at the critical angle for P-wave diffraction, generating the Pd portion of SPdKS, is indicated by the yellow circle and the is *Pd inception* point. Many data in this study have Pd inception points before encountering the ULVZ as drawn in green. (b) Collected SPdKS paths are displayed (total of 4221 records). Green stars (earthquakes), blue triangles (receivers), and great-circle ray paths (dashed black lines) are shown with the Pd segments of SPdKS (thick red lines) and SKPdS (thick blue lines) predicted by the PREM (Dziewonski and Anderson, 1981) model. (For interpretation of the references to color in this figure legend, the reader is referred to the web version of this article.)

Pd energy sends P energy into the core along entire Pd segments, a single SPdKS is composed of any number of combinations of core versus receiver-side Pd segments (Choy et al., 1980); the nomenclature SPdKS is thus meant to represent all viable possibilities of SPdKS (source-side Pd) and SKPdS (receiver-side Pd) for any source-receiver geometry.

We refer to the point where Pd initiates on the source-side of the ray path for phase SPdKS as the *Pd-inception point*. For average mantle properties, SPdKS first occurs at epicentral distances near 104° (exact distance depends on event source depth), yet the arrival is nearly coincident in time with SKS and does not appear as a distinct arrival until distances near 110°, where SPdKS trails SKS. For an SPdKS wave recorded at 110° the Pd portion of the wavepath along the CMB is approximately 360 km. For an SPdKS wave recorded at 125° the Pd portion of the wavepath along the CMB is approximately 1275 km. Previous efforts have noted that SPdKS waveform effects caused by ULVZs are maximized for records at epicentral distances of roughly 110–112° where SPdKS first emerges and the Pd path lengths are the shortest (Thorne and Garnero, 2004). As the distance increases beyond that, the waveforms behave more similarly to average mantle properties. This is due in part to interfering waves, i.e., SKS and SPdKS at smaller distances, having a more pronounced waveform effect, and in part due to longer Pd paths sampling a progressively larger vertical and lateral scale of D″, and hence, the ULVZ plays a smaller role in perturbing the wavefield. The lateral scale lengths of imaged ULVZs in some locations appear to be on the order of 10's of km (Idehara, 2011; Idehara et al., 2007; Rost et al., 2006). Thus, resolution of small scale ULVZ properties in previous studies has entailed analysis of SPdKS records at epicentral distances less than roughly 115° where the Pd paths are short enough to resolve fine-scale ULVZ structure.

Most seismic probes of ULVZ structure (e.g., ScP, PcP, ScS, and PKP precursors) interact with ULVZs at the CMB reflection or transmission location (Hutko et al., 2009; Rost et al., 2005; Thomas et al., 1999). As a result, studies using these seismic phases provide information about ULVZs in limited geographic locales. SPdKS, however, is sensitive to ULVZ properties over larger lateral spatial scales because of the horizontally propagating Pd segments, but can average or blur structure, especially for longer Pd segments. In this study, we show that SPdKS is strongly sensitive to ULVZ location along the Pd arc. And thus, SPdKS has the ability to constrain ULVZ location (similar to probes like ScP and PcP) but can be used to locate ULVZs over larger spatial extents due to the large lengths of the Pd arcs.

We gathered SKS and SPdKS waveforms from 51 high quality deep earthquakes in the Tonga–Fiji–Kermadec and Java trench regions, recorded at broadband seismic stations around the globe (Fig. 1b), resulting in 4221 total high quality vertically polarized shear wave records between epicentral distances of 90–125°. This corresponded to 2434 SKS records (90–104°) and 1787 SKS+SPdKS waveforms (104–125°). Our criteria for selecting events were as follows: (1) Source depth $\geq$100 km in order to eliminate interference with depth phases, (2) Data must exist for SPdKS waveforms in the distance range $104^\circ \leq \Delta \leq 125^\circ$, (3) The source-time function must be impulsive and simple, and (4) we must be able to unambiguously identify SKS. With respect to criterion (3), we analyzed the source-time function by comparing SKS waveforms at epicentral distances $\leq 110^\circ$ with Hilbert transformed SKKS waveforms. The importance of this step is to ensure that source-time function or receiver effects are not being interpreted as SPdKS waveform behavior. With respect to criterion (4), each individual seismic trace was overlain with a synthetic seismogram computed for the PREM (Dziewonski and Anderson, 1981) model. For each trace the seismic phases SKS and SKKS were identified (and Sdiff for distances where it is noticeable in the SV-wavefield). If the phases SKS and SKKS were not clearly

identifiable the trace was discarded. If no traces remained in our targeted distance range the event was discarded.

## 3. Method

Most studies that compare ULVZ data to predictions compute synthetic waveforms from models that vary solely with depth (1D) (Garnero and Helmberger, 1998; Rost et al., 2006; Thorne and Garnero, 2004). In order to investigate more realistic ULVZ morphologies, we employed an axi-symmetric spherical Earth finite difference method that permits SKS/SPdKS synthetic seismogram computation with dominant periods down to 6 sec for models that vary in the direction of wave propagation. We have updated a 2.5D axi-symmetric finite difference code (PSVaxi) for simulating seismic wave motion for distributed memory computer systems, allowing for the computation of SPdKS waveforms at broadband frequencies for 2D model geometries. The 2D model is expanded to 3D by virtually rotating the model around the axis passing through the source and the center of the earth. This technique thus provides correct 3D geometric spreading for a 2D input model. As this is a combination between a 2- and 3D technique we refer to the method as a 2.5D technique throughout this paper. The method is based on the technique previously developed by Igel and Weber (Igel and Weber, 1996) which we have extended to utilize supercomputer architecture (Jahnke et al., 2008; Thorne et al., 2007; Thorne et al., in press).

We explored 100's of models with the ULVZ located on the source-side of the path, i.e., in the Pacific LLSVP, motivated from previous work demonstrating the low likelihood of ULVZ structure on the receiver-side of the SKS/SPdKS wave paths for our study area of focus (Thorne and Garnero, 2004). Our model space included ULVZs with standard 1D parameters: (1) reduction is *S*-wave velocity ($\delta V_S$), (2) reduction in P-wave velocity ($\delta V_P$), (3) density contrast ($\delta\rho$), and (4) ULVZ thickness ($h$), as well as additional 2D parameters: (5) ULVZ length, and (6) ULVZ position relative to the SKS and SPdKS wave fields. The ULVZ spatial parameters used are displayed in Fig. 2. It is important to note that, for our 2D input models we also investigate the effect of Pd inception locations being either within or outside of the ULVZ. Table 1 summarizes the model space explored in this study.

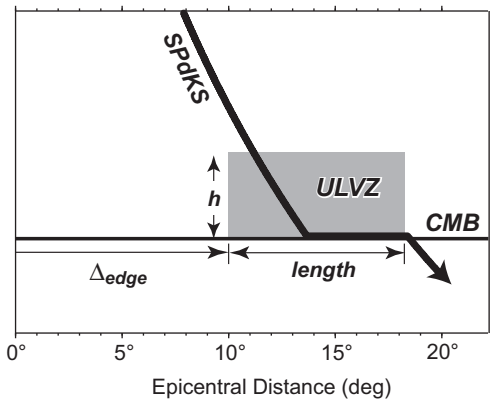


**Fig. 2.** 2D ULVZ spatial properties. ULVZ models are described spatially by their thickness ($h$), length in the great circle arc direction (*length*), and position ($\Delta_{edge}$) of the ULVZ leading edge with respect to the location of the source (located at 0°). The ULVZ (gray box) in this example has a length of 8° and an edge position of 10°. An example SPdKS ray path for a 400 km source depth and a 108° epicentral distance is drawn in with the heavy black line.

## 4. Results

The majority of previous studies analyzing SPdKS data have synthesized waveforms using a 1D technique such as reflectivity (Kind and Müller, 1975). In such 1D modeling efforts ULVZ structure is located on both source- and receiver-sides of the SPdKS/SKPdS ray paths. This has strong implications on inferred ULVZ properties if for example, ULVZ structure is only found on the source-side of the ray path. Fig. 3 shows a comparison of synthetic seismograms computed with PSVaxi for models with ULVZ structure at both the source- and receiver-sides (effectively 1D models) and for models with ULVZ structure solely located on the source-side (2.5D models). Pronounced differences between 1D and 2.5D models are apparent; in particular, the 1D models show an earlier emergence of SPdKS than in the 2.5D models. Waveform effects are most pronounced at distances where SPdKS first emerges from SKS, but at longer distances 1D models also show larger SPdKS travel-time delays with respect to SKS. In order to reproduce the waveform and timing characteristics of the 1D results with the 2.5D synthetics (with source-side ULVZ only), the ULVZ lateral and vertical dimensions and/or the magnitude of the ULVZ velocity reductions must be increased (beyond that in the 1D model). Thus, previous 1D modeling efforts may have underestimated either ULVZ thickness or the magnitude of the velocity reductions (or both).

For models without ULVZ structure, SPdKS does not appear as a distinct arrival in waveforms until beyond around 110°, where it emerges after SKS. SPdKS is most diagnostic of ULVZ structure at slightly smaller distances, where Pd segments are short, e.g., 104° to 110°; our data set includes 507 records in this distance range. We observe three distinct classes of SKS/SPdKS waveform behavior: (1) SKS and SPdKS agree with models lacking ULVZ structure (Fig. 4a); (2) SKS is significantly broadened with additional arrivals in its shoulders, consistent with ULVZ presence, called Type A (Fig. 4b); and (3) SPdKS is fully developed as a distinct arrival, also consistent with ULVZ presence (called Type B, Fig. 4c). Fig. 4d shows where Pd initiates on the source-side of the SPdKS

**Table 1**
Small scale ULVZ models explored (widths 1.5–12.0°).

| $\delta V_S$ (%) | $\delta V_P$ (%) | $d\rho$ (%) | $h$ (km) | Length (deg) | Length (km on CMB) | Edge* (deg) |
|---|---|---|---|---|---|---|
| −15 | −5 | +10 | 10, 20, 40 | 1.5, 3.0, 6.0, 12.0 | 91, 182, 364, 728 | 10.0, 11.5, 13.5, 14.0, 16.0, 17.5 |
| −30 | −10 | +10 | 10, 12, 15 20, 40 | 1.5, 3.0, 4.5 | 91, 182, 273 | 10.0, 11.5, 13.5, 14.0, 16.0, 17.5 |
| −30 | −10 | +10 | 10 | 6.0, 12.0 | 364, 728 | 10.0, 11.5, 13.5, 14.0 16.0, 17.5 |
| −45 | −15 | +10 | 10, 12, 15, 20, 40 | 1.5, 3.0, 4.5 | 91, 182, 273 | 10.0, 11.5, 13.5, 14.0, 16.0, 17.5 |
| −45 | −15 | +10 | 10 | 6.0, 12.0 | 364, 728 | 10.0, 11.5, 13.5, 14.0, 16.0, 17.5 |

* Note that the Pd inception point for the PREM model occurs at roughly 13.6°.

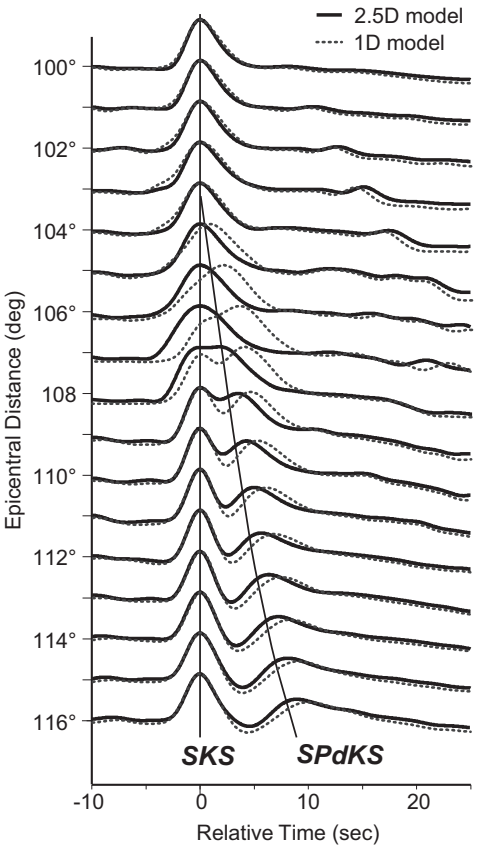


**Fig. 3.** Comparison between 1D and 2.5D ULVZ models. Shown are synthetic seismograms with ULVZ solely on the source-side of the SPdKS ray paths (black traces) and with ULVZ on both source- and receiver-sides (SPdKS+SKPdS) of the ray paths (dotted lines). Shown are radial component displacement seismograms, aligned and normalized to unity on the SKS arrival. Seismograms are computed for a ULVZ model with properties: $\delta V_S = -18\%$; $\delta V_P = -6\%$; $\delta\rho = +10\%$; $h = 10$ km. The source-side only ULVZ model has a length $= 40^\circ$ and edge $= 1^\circ$.

ray path (the Pd-inception point) for all data between 104–110°. Data lacking evidence for ULVZ structure are distributed throughout our study area, but most concentrated in the west (longitudes 160–185°). Type A waveforms are sporadically observed in the west, but more concentrated in the east (longitudes 180–200°). A striking feature in Fig. 4d is the tight cluster of Type A and B waveforms near the center of the Pacific LLSVP (near 190° longitude), where the LLSVP appears to be locally absent, i.e., the anomalously low shear velocities characteristic of LLSVP structure transition to normal velocities in this location.

Our synthetic tests demonstrate that Type B waveform shapes are highly sensitive to how much of the Pd segment in SPdKS is in normal mantle before encountering the ULVZ, and thus provides crucial information on the location of the edge of the ULVZ relative to the Pd-inception point. Examination of longer distance SPdKS waveforms (e.g., $>110^\circ$) provides a constraint on the length of the ULVZ in the direction of the great circle wave path. Combining Type B waveform information with differential times between SKS and SPdKS permits the constraint of both ULVZ location and lateral extent.

Observations were grouped according to small rectangular geographical areas ("bins") of Pd-inception point locations, and compared to a library of synthetic seismogram predictions constructed from a large suite of models. Our gathers are constructed for geographical bin sizes of $2.5^\circ \times 2.5^\circ$. Supplemental on-line material shows all data bins used in this study along with all data that went into these bins. Data bins characterized by normal waveforms (for distances between 104° and 110°), are well fit by synthetic predictions for the PREM model (Dziewonski and Anderson, 1981), a standard reference Earth model lacking a ULVZ (Fig. 5a). Type A waveforms (Fig. 5b) have three distinct arrivals: SPKS, a precursor to SKS, where the down-going S-wave converts to a P-wave at the top of ULVZ before entering the core, the main SKS phase, and SPdKS, which emerges as a postcursory shoulder to SKS. For the range of models explored, Type A waveforms were reproduced only when Pd inception points occur inside the ULVZ (or very close to the ULVZ edge), which permits an S-to-P conversion and generates SPKS. Type A waveforms are readily identified when ULVZ properties contain significant S- and P-wave velocity reductions or increased thickness. For smaller ULVZ velocity reductions and/or smaller thickness SPKS arrives too close in time to the SKS arrival and is typically indistinguishable from SKS. SPKS can be observed in 1D ULVZ models, however its importance in 2.5D modeling is that its presence provides direct constraint on ULVZ position. Type B contains as many as three distinct arrivals: SKS, SPdKS, and SpPKS, the latter being a post-cursor to SPdKS where P-wave energy is multiply reflected inside the ULVZ. For Type B data, waveforms are best matched when Pd inception locations are clearly outside of the ULVZ with the Pd path extending into the ULVZ (Fig. 5c).

For comparison of synthetic seismograms with data, we gather all data, regardless of epicentral distance, in common bins based on the Pd-inception point. Once data are sorted into geographic bins, there are often several traces recorded at similar epicentral distances. We next stack traces (for each geographic bin) into 2° epicentral distance bins. We compare synthetic seismograms for each model to stacked data traces by (a) calculating a correlation coefficient between each stacked trace and synthetic seismograms at the same distance, and (b) averaging the correlation coefficients of each trace/synthetic pair for that model. This process results in a single number that represents how well a particular ULVZ model fits the data at all epicentral distances in a single geographic bin. Because we use equal weight for data and synthetics at all epicentral distances our final ULVZ model must explain both early distance records (e.g., in the range 105° to 110°) where Type A and B waveform behavior may be present and records at longer distances (e.g., as far as 120°) where relative timing between SPdKS and SKS must be duplicated. The importance of these two constraints is manifest when modeling data that shows Type A or B waveform behavior. In particular, (a) large enough velocity reductions must be present in the ULVZ model to reproduce the Type A and B waveform behavior, which must be balanced with (b) the lateral size and thickness of the ULVZ model that must not be too large in order to maintain SPdKS relative time delays that are not excessively large.

Examination of data versus synthetics in this manner shows extreme sensitivity of ULVZ location with respect to Pd-inception. Once a best-fit model is constrained, with both ULVZ length and position determined with respect to Pd-inception, we plot the inferred ULVZ locations on a map. Our processing steps are summarized as: (1) determine the best fitting ULVZ model for each geographic bin, (2) determine the average event to receiver azimuth of SPdKS rays for this geographical bin, and (3) offset the correct size ULVZ in the direction of the average event to receiver azimuth. Thus we place the best-fitting ULVZ model in its appropriate location on the map.

Fig. 6 shows an example of data and synthetic seismograms collected for one geographic bin (bin number: 0813). Fig. 6a shows all data collected (gray traces) with 2° epicentral distance stacks superimposed (red traces). For this example, records between 105° and 110° consistently show Type B waveform behavior. Fig. 6b shows the data stacks (red traces) overlain on

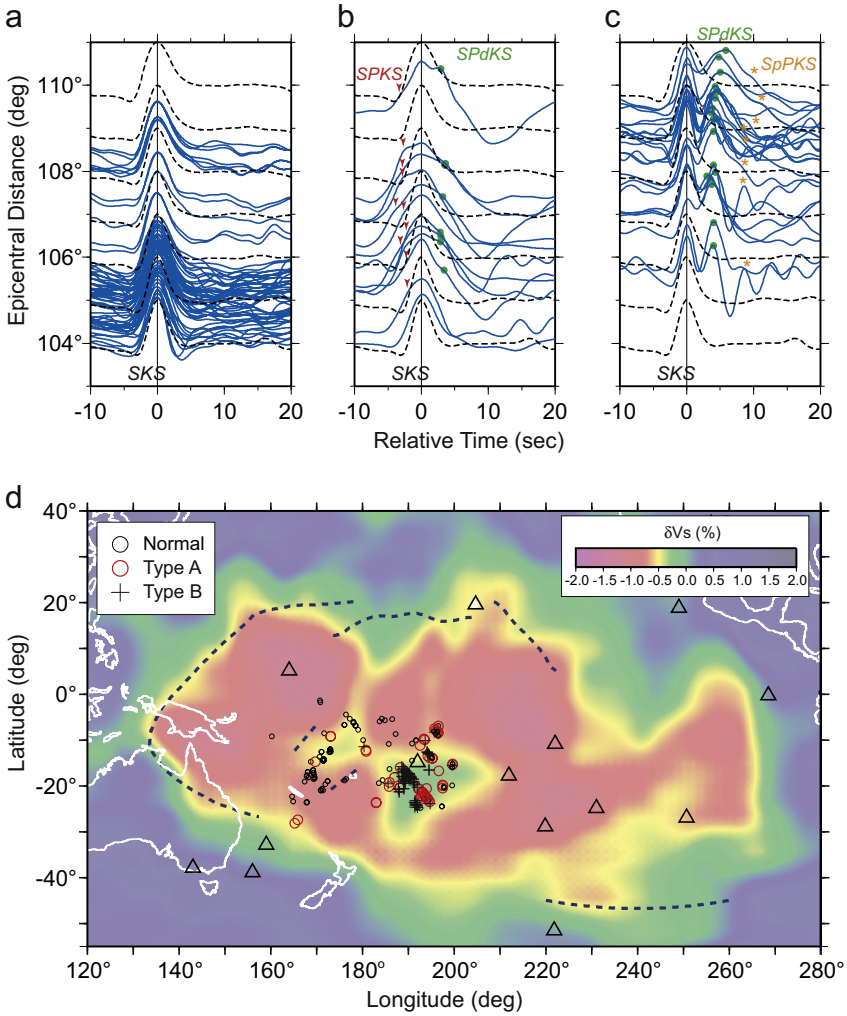


**Fig. 4.** Data classification. Shown are radial component displacement waveform examples aligned and normalized to unity on the SKS peak, between epicentral distances $104^\circ \leq \Delta \leq 110^\circ$. Blue traces are data and dashed black traces are synthetic seismograms computed for the 1-D PREM model. (a) Normal waveforms: SKS is the only apparent arrival [for a 160 km wide data bin centered at: 171.25°, −13.75°]. (b) Type A waveforms. Apparent arrivals are SPKS, a precursor to SKS due to the ULVZ (inverted orange triangles), SKS (aligned on zero time), and SPdKS (green circles) [160 km wide data bin centered at: 193.75°, −21.25°]. (c) Type B waveforms. Apparent arrivals are SKS (at zero time), SPdKS (green circle), and SpPKS, an SKS wave that has 1 internal reverberation in the ULVZ (orange star) [160 km wide data bin centered at: 191.25°, −23.75°]. (d) Map with location of Pd-inception points for all data between epicentral distances: $104^\circ \leq \Delta \leq 110^\circ$ (total of 507). Pd-inception points are coded as: Normal (open black circles), Type A (open orange circles), and Type B (black crosses). The surface locations of hot spots are shown as open black triangles (Steinberger, 2000). The background is shaded by S-wave tomography model TXBW in the lowermost mantle (Grand, 2002). Dashed blue lines show the inferred boundaries of the Pacific LLSVP from forward modeling studies (see Supplementary information for details on hot spot catalog and studies inferring LLSVP boundaries). (For interpretation of the references to color in this figure legend, the reader is referred to the web version of this article.)

synthetic seismograms computed for the PREM model (gray traces). Synthetics computed for the PREM model are incapable of replicating the waveform behavior observed here. Most notably, the Type B waveform behavior, with emergence of SPdKS at distances $<112^\circ$, and the travel time delay between SPdKS and SKS at larger distances is not reproduced. Fig. 6c shows these data stacks overlain on synthetic seismograms for the best-fit ULVZ model (gray traces). The best-fit ULVZ model captures the Type B waveform behavior observed in this data bin and also explains the SPdKS-SKS differential times. Nonetheless, differences between data and synthetics remain, primarily at the shortest distances (near 106°). These differences are primarily due to the extreme sensitivity of Pd-inception point with respect to ULVZ edge location. In particular, this demonstrates the balance between (a) using geographic bins large enough to be able to make data/synthetic comparisons at the full epicentral distance range, with (b) possible sub-bin size ULVZ variations. Fig. 6d shows the direction of Pd ray paths along the CMB for these data. Because these ray paths all trend to the northeast, the location of the ULVZ is placed along the average ray path direction (trending 55° clockwise from north in this example). A cross section of the best-fit ULVZ model for this bin is shown in Fig. 6e. This ULVZ model has an edge location that is 1.5° larger in angular distance than the Pd-inception point. Hence, our ULVZ model (magenta shaded region in Fig. 6d) is displaced 1.5° to the northeast of the Pd-inception points for this geographic bin. Supplementary online material shows all data used in this study grouped by geographic bin and shows the best-fit ULVZ model in plots similar to Fig. 6.

The resulting ULVZ distribution is shown in Fig. 7a. The main feature is a contiguous mega-sized ULVZ approximately 800 km in length and 250 km wide. The ULVZ edges on the east and west sides (lined in solid black, Fig. 7a) are well resolved, however there is not enough data to constrain the southern and northeastern boundary. There is some evidence this ULVZ may terminate on the southern boundary; a possible continuation of the ULVZ to the northwest cannot be precluded, due to lack of data sampling there. This is the largest ULVZ imaged to date (by an order of magnitude) using high-resolution techniques.

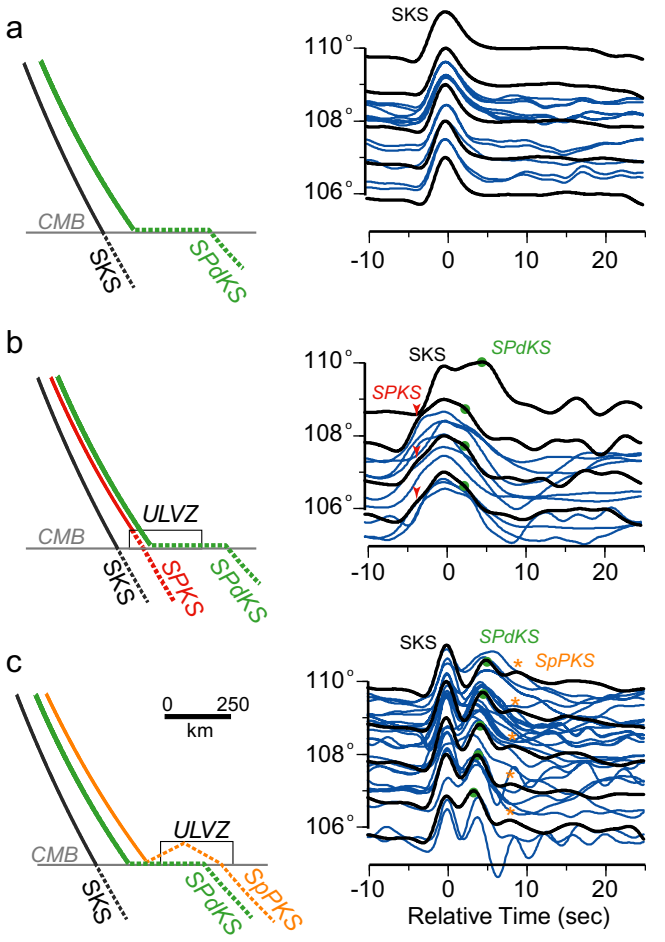


**Fig. 5.** Observations and synthetic predictions. *Left hand column*: ray path diagram of visible seismic phases for each data type. *Right hand column*: radial component displacement waveforms normalized in time and amplitude to SKS. Data (blue traces) and synthetics (black traces) correspond to the geographic bins in Fig. 2. Synthetic seismograms are calculated for: (a) Normal waveforms: PREM model. (b) Type A waveforms: ULVZ model with S-velocity reduction = −45%, P-velocity reduction = −15%, density increase = 10%, thickness = 10 km, and length = 290 km. The edge of the ULVZ is located 11.5° from the source position. (c) Type B waveforms: ULVZ model as in (b), but with length = 194 km and ULVZ edge position = 14.5°. (For interpretation of the references to color in this figure legend, the reader is referred to the web version of this article.)

We note that the boundaries drawn in Fig. 7a are for the best-fit model obtained using the methods outlined above. However, some uncertainty exists in the borders as displayed in this figure. Our data are gathered into 2.5° × 2.5° geographic bins and our synthetic model space is discretized in 1.5° increments in both ULVZ length and ULVZ position. Hence the boundaries drawn in Fig. 7a could be in error of up to approximately 3.0° (~180 km) in the worst case scenario where Pd-inception points are located near the extreme boundary of the geographic bin and true ULVZ edge position is midway between discrete intervals. An additional complication is the presence of multiple ULVZs in close proximity to each other. For example, records with Pd-inception located at roughly 188° longitude and −18° latitude (see Fig. 7a) display Type B waveform characteristics, but appear more complicated than in other bins. This is likely due to some interaction of the wavefield with a prominent ULVZ immediately to the southwest. As our model space does not include multiple ULVZs further uncertainty may be introduced into our model on this basis as well.

Tradeoffs always exist in the model space when examining SPdKS records (Garnero and Helmberger, 1998). Introducing a 2D model space introduces additional tradeoffs such as a tradeoff between ULVZ thickness and ULVZ length. As a result one may expect multiple ULVZ models to explain these data equally as well. An example of how different models fit these data is shown in supplementary online materials. In general, these data may be fit with different classes of models (e.g., $\delta V_S = -45\%$ and $\delta V_P = -15\%$ or $\delta V_S = -30\%$ and $\delta V_P = -10\%$). In this case, additional information such as such as the delta-inception distance described below, or the presence or lack of additional arrivals such as SPKS are necessary to help constrain which model class is most likely. Nevertheless, the presence of Type A and B waveforms provides us with confidence that our boundaries are close to their true position as the existence of these waveforms is dependent upon their interaction with a ULVZ.

The epicentral distance at which SPdKS initiates (referred to as delta-inception distance) helps to constrain ULVZ P-velocity (Rondenay et al., 2010), but dense data sampling is required to accurately determine this distance and has not been done in previous studies. We have seven geographical bins with dense enough sampling of Type B records which we use to extrapolate a delta-inception distance from 98° to 99.5°, suggesting a P-wave velocity reduction between 13.5% and 16.7%, averaging ~15% reduction. This is consistent with that inferred from SKKS/SKS amplitude ratio anomalies, which infer a 10–20% reduction in a 10–20 km thick ULVZ layer (Zhang et al., 2009). Our data are well explained with S-velocity reductions of 45%; the 3:1S-to-P velocity reduction implies the presence of partial melt (Williams and Garnero, 1996), although we do not specifically resolve the 3:1 velocity ratio with these data, since the SPdKS data have stronger sensitivity to the P-velocity structure.

In addition to large ULVZ displayed in Fig. 7a, four smaller patches of ULVZ are also identified. Data scarcity in these locations precludes a clear determination of size and boundaries of these ULVZs. An additional ULVZ, not illustrated, may be located near -15° latitude and 200° longitude: at this location there are two records demonstrating distinct Type A waveforms and an additional record demonstrating Type B waveform behavior. However, we do not specify a ULVZ in this location because of four collocated normal waveforms. It is possible a relatively small, sub-bin-sized patch of ULVZ material is located there, which only affects some of the records.

One previous study (Wen and Helmberger, 1998) examined the effect of ULVZ shape on SPdKS waveforms, testing both boxcar shaped ULVZs, as in this study, and dome shaped ULVZs. This study noted distinct differences in amplitude for records between 111° and 115° in epicentral distance, although the same general waveform characteristics were observed. We did not examine the effect of dome shaped ULVZs, but motivated by recent geodynamic work (Hernlund and Jellinek, 2010; McNamara et al., 2010) tested the effect of trapezoidal shaped ULVZs. We observed the strongest waveform effect on Type A waveforms. This is because the timing of the precursory energy generated by the SPKS phase is strongly dependent on ULVZ thickness. Thus lateral variation in ULVZ thickness can strongly affect when SPKS arrives with respect to the SKS arrival and thus whether or not SPKS is distinctly observable and recognizable as a Type A waveform. A possible consequence of trapezoidal shaped ULVZs is that the dimensions of our Mega ULVZ may indeed be larger, but that we are not capable of identifying Type A waveform behavior near the outermost edges of the ULVZ due to its reduced thickness. For Type B waveforms, the general waveform characteristics are the same for both boxcar and trapezoidal shaped ULVZs. However, timing of the SPdKS arrival is dependent on the location of the thickest portion of the trapezoid and not just the ULVZ edge. Future efforts should further investigate the SPKS phase in order to better constrain the ULVZ shape.

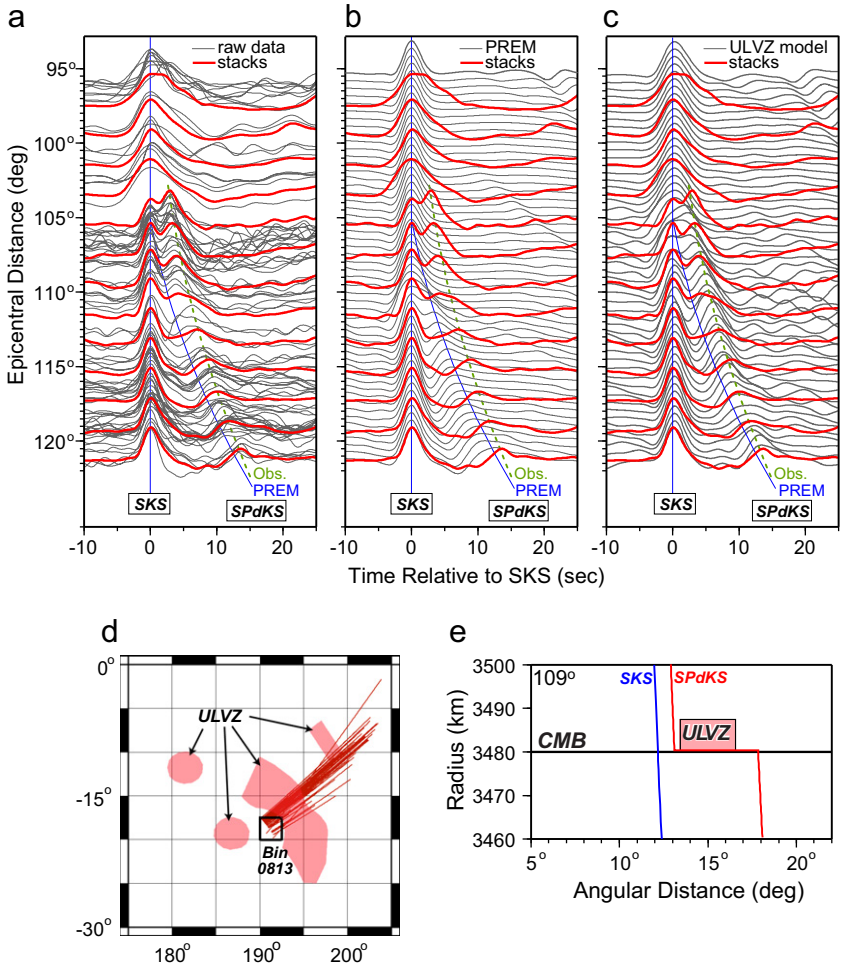


**Fig. 6.** Examination of data and synthetics for Bin 0813 centered at 191.25° longitude and −18.75° latitude. (a) All data with Pd-inception points inside this bin are shown (gray traces) aligned and normalized to unity on the SKS arrival. Data are stacked in 2° epicentral distance ranges (red traces). These data stacks are repeated in columns (b) and (c). The blue line shows the PREM predicted arrival time of SPdKS, and the dashed green line shows the arrival time of SPdKS for these data. (b) Data stacks (red traces) are compared with synthetic seismograms computed for the PREM model. (c) Data stacks (red traces) are compared with synthetic seismograms for the best-fit ULVZ model for this data bin. The ULVZ model has characteristics: $\delta V_S = -45\%$, $\delta V_P = -15\%$, $\delta\rho = +10\%$, $h = 7.5$ km, length = 4.5°, and edge = 13.0°. (d) Pd-segments (red lines) of SPdKS are shown for data in this bin (bin area outlined in black). For reference, the positions of ULVZs identified in this study are shaded in magenta. (e) Cross-section in the great circle arc distance of the best-fit ULVZ model (magenta shaded box) for this bin. Synthetics shown in panel (c) are computed for this ULVZ model geometry. For reference, SKS and SPdKS ray paths are shown for an epicentral distance of 109°. (For interpretation of the references to color in this figure legend, the reader is referred to the web version of this article.)

## 5. Discussion and conclusions

The mega-sized ULVZ imaged here is located in an apparent hole in the Pacific LLSVP (Figs. 4d and 7a); this hole is seen in other tomographic models and supported by detailed seismic waveform studies (He and Wen, 2009). Tomographically imaged LLSVPs have been hypothesized to be caused by the presence of compositional reservoirs, or thermochemical piles (Bull et al., 2009; McNamara and Zhong, 2005; Tackley, 2002). ULVZs are predicted to concentrate at thermochemical pile margins (McNamara et al., 2010); though if a pile splits into two, the new pile edges at the bifurcation location will lack ULVZ material (Hernlund and Tackley, 2007; McNamara et al., 2010). Conversely, when two piles merge, ULVZ material from the two merging pile edges combines, temporarily residing at the location where the piles meet. If thermochemical pile edges are sloped (Jellinek and Manga, 2002; McNamara et al., 2010), ULVZs merge first, and lack overlying pile material until the merging is complete, upon which ULVZ material migrates towards the edges of the single merged pile (Fig. 7b).

The observation of this mega-sized ULVZ located in an apparent hole in a LLSVP is consistent with the lower mantle beneath the Pacific Ocean being composed of two or more individual thermochemical piles that are currently in the process of merging. As individual piles merge, the thermal boundary layer along the tops of the merging thermochemical piles is disrupted, often resulting in anomalously large plumes that can entrain pile and ULVZ material. The deep mantle beneath the southwest Pacific has been attributed to being the source region for hot spot upwelling in the past, such as the Samoa hot spot, which directly overlies the mega-sized ULVZ (Courtillot et al., 2003; Montelli et al., 2006; Torsvik et al., 2006) imaged here. This region may also be associated with larger scale upwelling. Infrequent massive eruptions that define large igneous provinces (LIPs) may be a natural consequence of periodically merging lowermost mantle thermochemical piles. Certainly our study region has been attributed to past LIP production, e.g., the hypothesized source location of the Ontong Java Plateau (Kroenke et al., 2004). If thermochemical piles and/or ULVZs are reservoirs of isotopes thought to be sequestered in the deep mantle (Kellogg et al., 1999; Labrosse et al., 2007), infrequent pile merging and resulting reservoir break-up may explain only rare occurrences of eruption of certain isotopes (Jackson et al., 2010). Mega-sized ULVZs as imaged here may represent the precursor to the next cycle in large boundary layer disruption leading to a superplume event.

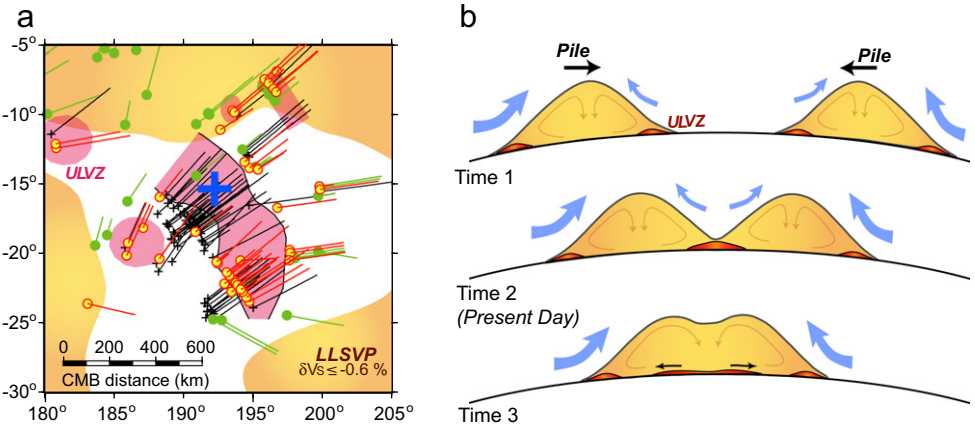


**Fig. 7.** ULVZ model and thermo-chemical pile dynamics. (a) The best-fitting solution for ULVZ geographic location and size is shown (magenta-shaded region). Constrained (solid black lines) and unconstrained (no solid line) ULVZ boundaries are indicated. Pd-inception points (symbols) and Pd arcs (connecting lines) are follows: Normal SPdKS data have green circles with green lines; Type A SPdKS data have yellow circles and red lines; Type B SPdKS data have black crosses and lines. ULVZ model properties are: S-wave velocity reduction = −45%, P-wave velocity reduction = −15%, density increase = 10%, thickness = 10–15 km. Background is colored such that orange and white areas represent S-wave velocities lower than and greater than −0.6% respectively in the tomography model TXBW (Grand, 2002). The blue cross shows the surface location of the Samoa hot spot. (b) Schematic cross-sections with two merging thermo-chemical piles for three time steps. Time 1—the piles (orange) are separated by some distance along the CMB and are merging in the direction as shown by the thick black arrows. ULVZs (red) are concentrated at the pile boundaries. Time 2—the piles begin to merge, resulting in two ULVZs combining into a single mega-sized ULVZ. This time step is consistent with the inferred present pile configuration and the mega-sized ULVZ we detect here. Time 3—The formerly distinct piles have merged into a single larger pile, with the central ULVZ material migrating back towards the pile boundaries (small black arrows indicate the direction of ULVZ motion). In each snapshot the thick blue arrows indicate the direction of mantle flow around the piles and the thin orange arrows indicate the direction of flow within the piles. (For interpretation of the references to color in this figure legend, the reader is referred to the web version of this article.)

## Acknowledgments

We thank the Arctic Region Supercomputing Center at the University of Alaska, Fairbanks and the Center for High Performance Computing at the University of Utah for use of their supercomputing facilities. MT was partially supported by NSF grant EAR-1014749. EJG was partially supported by EAR-0453944. AKM was partially supported by NSF grants EAR-0456356 and EAR-0510383. We also thank the Incorporated Research Institution for Seismology and EarthScope for the freely available data used in this study. We thank two anonymous reviewers whose comments strengthened this manuscript. We gratefully acknowledge support through the EU project SPICE.

## Appendix A. Supporting information

Supplementary data associated with this article can be found in the online version at http://dx.doi.org/10.1016/j.epsl.2012.12.034.

## References

Becker, T.W., Boschi, L., 2002. A comparison of tomographic and geodynamic mantle models. Geochem. Geophys. Geosyst. 3.
Berryman, J.G., 2000. Seismic velocity decrement ratios for regions of partial melt in the lower mantle. Geophys. Res. Lett. 27, 421–424, http://dx.doi.org/10.1029/1999GL008402.
Bréger, L., Romanowicz, B., 1998. Three-dimensional structure at the base of the mantle beneath the Central Pacific. Science 282, 718–720, http://dx.doi.org/10.1126/science.282.5389.718.
Bull, A.L., McNamara, A.K., Ritsema, J., 2009. Synthetic tomography of plume clusters and thermochemical piles. Earth Planet. Sci. Lett. 278, 152–162, http://dx.doi.org/10.1016/j.epsl.2008.11.018.
Burke, K., 2011. Plate tectonics, the Wilson Cycle, and mantle plumes: geodynamics from the top. Ann. Rev. Earth Planet. Sci. 39, 1–29, http://dx.doi.org/10.1146/annurev-earth-040809-152521.
Choy, G.L., Cormier, V.F., Kind, R., Müller, G., Richards, P.G., 1980. A comparison of synthetic seismograms of core phases generated by the full wave theory and by the reflectivity method. Geophys. J. R. Astron. Soc. 61, 21–39.
Courtillot, V., Davaille, A., Besse, J., Stock, J., 2003. Three distinct types of hotspots in the Earth's mantle. Earth Planet. Sci. Lett. 205, 295–308.
Deschamps, F., Tackley, P.J., 2009. Searching for models of thermo-chemical convection that explain probabilistic tomography. II—Influence of physical and compositional parameters. Phys. Earth Planet. Inter 176, 1–18, http://dx.doi.org/10.1016/j.pepi.2009.03.012.
Dziewonski, A.M., Anderson, D.L., 1981. Preliminary reference Earth model. Phys. Earth Planet. Inter 25, 297–356.
Ford, S.R., Garnero, E.J., McNamara, A.K., 2006. A strong lateral shear velocity gradient and anisotropy heterogeneity in the lowermost mantle beneath the southern Pacific. J. Geophys. Res., 111, http://dx.doi.org/10.1029/2004JB003574.
Garnero, E.J., Helmberger, D.V., 1998. Further structural constraints and uncertainties of a thin laterally varying ultralow-velocity layer at the base of the mantle. J. Geophys. Res. 103, 12495–12509.
Garnero, E.J., McNamara, A.K., 2008. Structure and dynamics of Earth's lower mantle. Science 320, 626–628, http://dx.doi.org/10.1126/science.1148028.
Grand, S.P., 2002. Mantle shear-wave tomography and the fate of subducted slabs. Philos. Trans. R. Soc. London A 360, 2475–2491, http://dx.doi.org/10.1098/rsta.2002.1077.
Gu, Y.J., Dziewonski, A.M., Su, W., Ekström, G., 2001. Models of the mantle shear velocity and discontinuities in the pattern of lateral heterogeneities. J. Geophys. Res. 106, 11,169–111,199.
He, Y., Wen, L., 2009. Structural features and shear-velocity structure of the "Pacific Anomaly". J. Geophys. Res., 114, http://dx.doi.org/10.1029/2008JB005814.
He, Y., Wen, L., Zheng, T., 2006. Geographic boundary and shear wave velocity structure of the "Pacific anomaly" near the core–mantle boundary beneath western Pacific. Earth Planet. Sci. Lett. 244, 302–314, http://dx.doi.org/10.1016/j.epsl.2006.02.007.
Hernlund, J.W., Jellinek, A.M., 2010. Dynamics and structure of a stirred partially molten ultralow-velocity zone. Earth Planet. Sci. Lett. 296, 1–8, http://dx.doi.org/10.1016/j.epsl.2010.04.027.
Hernlund, J.W., Tackley, P.J., 2007. Some dynamical consequences of partial melting in Earth's deep mantle. Phys. Earth Planet. Inter. 162, 149–163.
Hofmann, A.W., 1997. Mantle geochemistry: the message from oceanic volcanism. Nature 385, 219–229.
Hutko, A.R., Lay, T., Revenaugh, J., 2009. Localized double-array stacking analysis of PcP: D″ and ULVZ structure beneath the Cocos plate, Mexico, central Pacific, and north Pacific. Phys. Earth Planet. Inter. 173, 60–74, http://dx.doi.org/10.1016/j.pepi.2008.11.003.
Idehara, K., 2011. Structural heterogeneity of an ultra-low-velocity zone beneath the Philippine Islands: implications for core–mantle chemical interactions induced by massive partial melting at the bottom of the mantle. Phys. Earth Planet. Inter. 184, 80–90, http://dx.doi.org/10.1016/j.pepi.2010.10.014.
Idehara, K., Yamada, A., Zhao, D., 2007. Seismological constraints on the ultralow velocity zones in the lowermost mantle from core-reflected waves. Phys. Earth Planet. Inter. 165, 25–46, http://dx.doi.org/10.1016/j.pepi.2007.07.005.
Igel, H., Weber, M., 1996. P-SV wave propagation in the Earth's mantle using finite differences: application to heterogeneous lowermost mantle structure. Geophys. Res. Lett 23, 415–418.

Ishii, M., Tromp, J., 2004. Constraining large-scale mantle heterogeneity using mantle and inner-core sensitive normal modes. Phys. Earth Planet. Inter 146, 113–124, http://dx.doi.org/10.1016/j.pepi.2003.06.012.

Jackson, M.G., Carlson, R.W., Kurz, M.D., Kempton, P.D., Francis, D., Blusztajn, J., 2010. Evidence for the survival of the oldest terrestrial mantle reservoir. Nature 466, 853–856, http://dx.doi.org/10.1038/nature09287.

Jahnke, G., Thorne, M.S., Cochard, A., Igel, H., 2008. Global SH-wave propagation using a parallel axisymmetric spherical finite-difference scheme: application to whole mantle scattering. Geophys. J. Int., http://dx.doi.org/10.1111/j.1365-246X.2008.03744.x.

Jellinek, A.M., Manga, M., 2002. The influence of a chemical boundary layer on the fixity, spacing and lifetime of mantle plumes. Nature 418, 760–763.

Jellinek, A.M., Manga, M., 2004. Links between long-lived hot spots, mantle plumes, D″, and plate tectonics. Rev. Geophys., 42, http://dx.doi.org/10.1029/2003RG000144.

Kellogg, L.H., Hager, B.H., van der Hilst, R.D., 1999. Compositional stratification in the deep mantle. Science 283, 1881–1884, http://dx.doi.org/10.1126/science.283.5409.1881.

Kind, R., Müller, G., 1975. Computations of SV waves in realistic Earth models. J. Geophys. 41, 149–172.

Kroenke, L.W., Wessel, P., Sterling, A., 2004. Motion of the Ontong Java Plateau in the hot-spot frame of reference: 122 Ma-present. In: Fitton, J.G., Mahoney, J.J., Wallace, P.J., Saunders, A.D. (Eds.), Origin and Evolution of the Ontong Java Plateau. Geological Society of London, London, pp. 9–20.

Labrosse, S., Hernlund, J.W., Coltice, N., 2007. A crystallizing dense magma ocean at the base of the Earth's mantle. Nature 450, 866–869, http://dx.doi.org/10.1038/nature06355.

Luo, S.-N., Ni, S., Helmberger, D.V., 2001. Evidence for a sharp lateral variation of velocity at the core-mantle boundary from multipathed PKPab. Earth Planet. Sci. Lett. 189, 155–164.

McNamara, A.K., Garnero, E.J., Rost, S., 2010. Tracking deep mantle reservoirs with ultra-low velocity zones. Earth Planet. Sci. Lett. 299, 1–9, http://dx.doi.org/10.1016/j.epsl.2010.07.042.

McNamara, A.K., Zhong, S., 2004. Thermochemical structures within a spherical mantle: superplumes or piles? J. Geophys. Res, 109, http://dx.doi.org/10.1029/2003JB002847.

McNamara, A.K., Zhong, S., 2005. Thermochemical structures beneath Africa and the Pacific Ocean. Nature 437, 1136–1139.

Mégnin, C., Romanowicz, B., 2000. The three-dimensional shear velocity structure of the mantle from the inversion of body, surface and higher-mode waveforms. Geophys. J. Int. 143, 709–728.

Montelli, R., Nolet, G., Dahlen, F.A., Masters, G., 2006. A catalogue of deep mantle plumes: new results from finite frequency tomography. Geochem. Geophys. Geosyst., 7, http://dx.doi.org/10.1029/2006GC001248.

Nakagawa, T., Tackley, P.J., Deschamps, F., Connolly, J.A.D., 2010. The Influence of MORB and harzburgite composition on thermo-chemical mantle convection in a 3-D spherical shell with self-consistently calculated mineral physics. Earth Planet. Sci. Lett. 296, 403–412, http://dx.doi.org/10.1016/j.epsl.2010.05.026.

Nomura, R., Ozawa, H., Tateno, S., Hirose, K., Hernlund, J.W., Muto, S., Ishii, H., Hiraoka, N., 2011. Spin crossover and iron-rich silicate melt in the Earth's deep mantle. Nature 473, 199–202, http://dx.doi.org/10.1038/nature09940.

Ritsema, J., van Heijst, H.-J., 2000. Seismic imaging of structural heterogeneity in Earth's mantle: evidence for large-scale mantle flow. Sci. Prog 83, 243–259.

Rondenay, S., Cormier, V.F., Van Ark, E.M., 2010. SKS and SPdKS sensitivity to two-dimensional ultralow-velocity zones. J. Geophys. Res., 115, http://dx.doi.org/10.1029/2009JB006733.

Rost, S., Garnero, E.J., Williams, Q., 2006. Fine-scale ultralow-velocity zone structure from high-frequency seismic array data. J. Geophys. Res., 111, http://dx.doi.org/10.1029/2005JB004088.

Rost, S., Garnero, E.J., Williams, Q., Manga, M., 2005. Seismological constraints on a possible plume root at the core–mantle boundary. Nature 435, 666–669, http://dx.doi.org/10.1038/nature03620.

Steinberger, B., 2000. Plumes in a convecting mantle: models and observations for individual hotspots. J. Geophys. Res. 105, 11,127–111,152.

Sun, D., Helmberger, D.V., Ni, S., Bower, D., 2009. Direct measures of lateral velocity variation in the deep Earth. J. Geophys. Res., 114, http://dx.doi.org/10.1029/2008JB005873.

Tackley, P.J., 2002. Mantle convection and plate tectonics: toward an integrated physical and chemical theory. Science 288, 2002–2007, http://dx.doi.org/10.1126/science.288.5473.2002.

Thomas, C., Weber, M., Wicks, C.W., Scherbaum, F., 1999. Small scatterers in the lower mantle observed at German broadband arrays. J. Geophys. Res. 104, 15073–15088.

Thompson, P.F., Tackley, P.J., 1998. Generation of mega-plumes from the core-mantle boundary in a compressible mantle with temperature-dependent viscosity. Geophys. Res. Lett 25, 1999–2002.

Thorne, M.S., Garnero, E.J., 2004. Inferences on ultralow-velocity zone structure from a global analysis of SPdKS waves. J. Geophys. Res., 109, http://dx.doi.org/10.1029/2004JB003010.

Thorne, M.S., Garnero, E.J., Grand, S.P., 2004. Geographic correlation between hot spots and deep mantle lateral shear-wave velocity gradients. Phys. Earth Planet. Inter. 146, 47–63.

Thorne, M.S., Lay, T., Garnero, E.J., Jahnke, G., Igel, H., 2007. Seismic imaging of the laterally varying D″ region beneath the Cocos Plate. Geophys. J. Int. 170, 635–648, http://dx.doi.org/10.1111/j.1365-246X.2006.03279.x.

Thorne, M.S., Zhang, Y., Ritsema, J. Evaluation of 1D and 3D seismic models of the Pacific lower mantle with S, SKS, and SKKS traveltimes and amplitudes. J. Geophys. Res. http://dx.doi.org/10.1002/jgrb.50054, in press.

To, A., Romanowicz, B., Capdeville, Y., Takeuchi, N., 2005. 3D effects of sharp boundaries at the borders of the African and Pacific superplumes: observation and modeling. Earth Planet. Sci. Lett. 233, 137–153.

Torsvik, T.H., Smethurst, M.A., Burke, K., Steinberger, B., 2006. Large igneous provinces generated from the margins of the large low-velocity provinces in the deep mantle. Geophys. J. Int. 167, 1447–1460, http://dx.doi.org/10.1111/j.1365-246X.2006.03158.x.

Trampert, J., Deschamps, F., Resovsky, J., Yuen, D.A., 2004. Probabilistic tomography maps chemical heterogeneities throughout the lower mantle. Science 306, 853–856, http://dx.doi.org/10.1126/science.1101996.

USArray. Available from: 〈http://www.earthscope.org/observatories/usarray〉 (accessed: 21.04.11).

Wen, L., Helmberger, D.V., 1998. A two-dimensional P-SV hybrid method and its application to modeling localized structures near the core-mantle boundary. J. Geophys. Res. 103, 17901–17918.

Williams, Q., Garnero, E.J., 1996. Seismic evidence for partial melt at the base of Earth's mantle. Science 273, 1528–1530.

Zhang, Y., Ritsema, J., Thorne, M.S., 2009. Modeling the ratios of SKKS and SKS amplitudes with ultra-low velocity zones at the core–mantle boundary. Geophys. Res. Lett., 36, http://dx.doi.org/10.1029/2009GL040030.